Nitrogen plasma formation through terahertz-induced ultrafast electron field emission

Iwaszczuk, Krzysztof; Zalkovskij, Maksim; Strikwerda, Andrew; Jepsen, Peter Uhd

Published in:
Optica

Link to article, DOI:
10.1364/OPTICA.2.000116

Publication date:
2015

Document Version
Publisher's PDF, also known as Version of record

Research Article Vol. 2, No. 2 / February 2015 / Optica 116

Nitrogen plasma formation through terahertz-induced ultrafast electron field emission

KRZYSZTOF IWASZCZUK,* MAKSIM ZALKOVSKIJ, ANDREW C. STRIKWERDA, AND PETER U. JEPSEN

DTU Fotonik—Department of Photonics Engineering, Technical University of Denmark, DK-2800 Kongens Lyngby, Denmark

**Corresponding author: kiwa@fotonik.dtu.dk*

Received 11 September 2014; revised 25 November 2014; accepted 27 November 2014 (Doc. ID 222904); published 30 January 2015

Electron microscopy and electron diffraction techniques rely on electron sources. Those sources require strong electric fields to extract electrons from metals, either by the photoelectric effect, driven by multiphoton absorption of strong laser fields, or in the static field emission regime. Terahertz (THz) radiation, commonly understood to be nonionizing due to its low photon energy, is here shown to produce electron field emission. We demonstrate that a carrier-envelope phase-stable single-cycle optical field at THz frequencies interacting with a metallic microantenna can generate and accelerate ultrashort and ultrabright electron bunches into free space, and we use these electrons to excite and ionize ambient nitrogen molecules near the antenna. The associated UV emission from the gas forms a novel THz wave detector, which, in contrast with conventional photon-counting or heat-sensitive devices, is ungated and sensitive to the peak electric field in a strongly nonlinear fashion.

OCIS codes: (190.7110) Ultrafast nonlinear optics; (240.6675) Surface photoemission and photoelectron spectroscopy; (300.6495) Spectroscopy, terahertz; (020.2649) Strong field laser physics; (350.5400) Plasmas.

http://dx.doi.org/10.1364/OPTICA.2.000116

1. INTRODUCTION

Femtosecond electron emission from metals can be induced by single- or multi-photon excitation of bulk metal with femtosecond laser pulses from amplified laser systems [1–3] or even with pulses directly from a femtosecond oscillator by exploiting the enhancement of the laser field at a nanotip [4–6]. Electron emission nanotips driven by femtosecond optical fields can be controlled by the carrier-envelope phase (CEP) of the field itself [7], or by an auxiliary long-wavelength optical field at terahertz (THz) frequencies [8]. Similarly, the tunnel current in a scanning tunneling microscope (STM) can be controlled by THz fields [9], potentially enabling femtosecond time resolution and atomic spatial resolution in the same instrument. The brightness of an ultrafast electron source is an important parameter for practical applications [2]. The absolute electron yield in photoemission processes varies from a few electrons per laser shot emitted from a single nanotip to approximately 10^5–10^6 electrons emitted from bulk metals irradiated by amplified femtosecond laser pulses. Whereas multiphoton-driven photoemission results in a narrow distribution of electron energies, field-driven emission results in a broad electron energy spectrum as electrons are emitted on a subcycle time scale, and subsequently accelerated by the optical field. In the latter case, the oscillation period strongly influences the energy spectrum of the electrons. Long oscillation periods lead to higher electron yield and higher energies. The wavelength dependence of electron emission from nanotips initiated by mid-IR pulses [10] showed that longer wavelengths are indeed favorable for acceleration of the emitted electrons by the optical field itself, however, with the caveat that the obtainable electron energy is limited by the extremely short range of the enhancement of the optical field [10]. In spite of this, the application of longer wavelength optical fields for electron emission will be favorable in terms of electron yield due to the significantly enhanced tunneling probability (lower Keldysh parameter) at lower field strengths.

2334-2536/15/020116-08$15/0$15.00

Here we explore the fundamental question of how long oscillation periods of an optical field we can apply in order to move deep into the extreme electrostatic limit of nonlinear optics and strong-field physics, while still maintaining femtosecond time resolution. We do so by using single-cycle optical fields at THz frequencies, and present the first demonstration, to the best of our knowledge, of a strong THz pulse causing direct ultrafast electron field emission from metal structures, without additional optical fields and with Keldysh parameters smaller than 10^{-2}. Through the use of microantennas, we have decreased the requisite intensity to induce field emission down to sub-GW/cm^2, which is below the damage thresholds of bulk materials and more than three orders of magnitude lower than previous work [4,5,7,10–12]. In spite of the comparably low intensity of the incident THz field, up to 10^7 electrons are emitted in a period of a few hundred femtoseconds, thus defining an extremely bright source of electrons synchronized to a femtosecond laser system. Furthermore we show that the liberated electrons acquire sufficient kinetic energy to generate nitrogen plasma through electron impact excitation and ionization of N_2 molecules. Through careful engineering, these liberated electrons could similarly be used to start various physical processes or chemical reactions that would otherwise be prohibitively disturbed by the presence of an intense laser field.

2. METHODS

A. Experimental Setup

Figure 1(a) shows the details of the experimental setup. A 5 mJ, 800 nm, 100 fs Ti:sapphire regenerative amplifier laser (Spitfire Ace) powers the system. High-power THz radiation is generated in a 1 mol. % MgO-doped stoichiometric $LiNbO_3$ crystal by optical rectification in a tilted wavefront phase matching configuration [13–16]. The THz pulse energy at the exit of the $LiNbO_3$ has been measured using a pyroelectric detector to be on a level of 1 μJ. The generated radiation is recollimated and focused onto the antenna array using a set of off-axis parabolic mirrors. Two wire grid polarizers W1 and W2 attenuate the THz beam without changing its linear polarization. The THz radiation has been characterized using electro-optic sampling [17–19] in a 300-μm-thick gallium phosphide (GaP) 110-cut crystal. At the sample position, THz peak electric fields of up to 200 kV/cm are obtained, with field strengths calibrated using combined information from free-space electro-optic sampling, pulse energy measurement, and spot size measurement [20]. The generated THz spectrum contains frequency components in the 0.1–2.5 THz range, with the amplitude reaching a maximum at 0.8 THz. The incident peak intensity of the THz beam at the sample spot is 0.1 GW/cm^2. The gold antennas are fabricated on 525-μm-thick high-resistivity silicon (HR-Si) substrates. HR-Si is transparent for THz radiation [21], but is opaque for wavelengths below its bandgap (approximately 1.1 μm). The sample is oriented so that the incoming THz radiation illuminates the substrate side first and the emitted UV radiation is detected on the opposite side, as shown in Fig. 1(a). The sample is in nitrogen atmosphere unless noted otherwise. All experiments are performed at room temperature. For the spectral measurement the generated UV radiation is collected by a fused-silica lens and imaged onto the entrance slit of a monochromator (McPherson 218). Photomultiplier tubes (PMTs) (Hamamatsu H5784-04, H5784, and R2496) sensitive in the range 180–850 nm are used as detectors. The UV emission spectra are adjusted for the wavelength-dependent responsivity of the PMT. The signal from the PMT is fed to a lock-in amplifier locked to the repetition rate of the Ti:sapphire laser.

To obtain information about the spatial profile of the samples' UV emission, a simple imaging system was built [Fig. 1(b)]. UV light is imaged using a single 60 mm focal length fused-silica glass lens with a magnification factor of 11× at the image plane. A 100 μm pinhole and a 10 nm bandpass filter centered at 340 nm (for the 337 nm line of the second positive system of N_2) are mounted on the PMT detector, which is raster scanned through the image plane. The imaging resolution of the assembly is 9 μm.

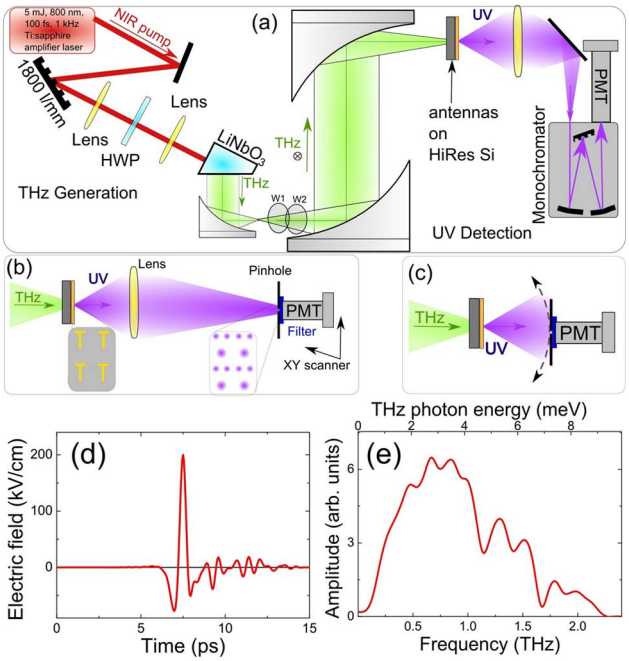

Fig. 1. (a) Schematic of the experimental setup. (b) Imaging setup for determination of the UV emission profile. (c) Determination of the emission directionality. (d) Time-domain waveform and (e) corresponding amplitude spectrum of the THz driving electric field at the sample.

B. Numerical Simulations

We performed full 3D time-domain simulations of the antenna structures with the commercial software package CST Microwave Studio. In the simulation, only a single unit cell is considered, and the array is enforced is by the boundary conditions—perfect electric conductors (PEC) and perfect magnetic conductors (PMC). Perfectly matched layers (PMLs) were used in the propagation direction. The gold antennas are treated as a lossy metal ($\sigma = 4.561 \cdot 10^7$ S/m), and silicon substrate was modeled as a lossless dielectric with a refractive index of 3.417. The structure is adaptively meshed with over $7 \cdot 10^6$ mesh cells, with the smallest mesh dimensions less than 10 nm. The experimentally obtained THz electric field

waveform [shown in Fig. 1(d)] is used as the input to the simulation. Since we use the electric field of the pulse, both the amplitude and phase of the incident wave are taken into account.

In the simulation, we monitor the value of the electric field in the plane of the antenna, in both time and frequency. As expected, we observe the highest field enhancement at the tips of the antennas. The field enhancement decreases away from the antenna tips with a characteristic length scale of 200 nm, which corresponds well to the smallest dimensions of the antenna (thickness of the gold layer).

C. Sample Design and Fabrication

Two shapes of antennas are explored, a symmetric I-shape [Fig. 2(a)] and a T-shape [Fig. 2(b)]. The asymmetric shape of the T-antenna has been chosen to investigate the symmetry properties of the field emission with regard to the polarity of the incident single-cycle THz electric field with respect to the antenna geometry and electron charge.

The samples were optimized for the highest field enhancement at the desired frequency. In the optimization process both the length of the antenna (L) and the period (P) of the array were varied, while the width of the antenna (w) and the gold thickness (d) have been kept constant at 5 μm and 200 nm. For the T-shape antennas, the length of the top bar is fixed at 1/2 of the antenna length. Figure 2 shows the optimized results for various resonant frequencies. Structures have been fabricated by standard UV lithography and the lift-off procedure of a 200-nm-thick electron beam-deposited gold layer on a dielectric substrate (high-resistivity silicon or fused-silica glass).

3. RESULTS

High-power THz transients are focused onto a sample of antenna arrays as shown in Fig. 1(a). When the antennas are exposed to these intense THz transients (photon energies 0.1–6 meV), a characteristic UV spectrum (photon energies 2.7–5 eV) is emitted, consisting of the emission lines of excited N_2 and singly ionized N_2^+ (Fig. 3). Even though the 391 nm emission line of N_2^+ is more than 20 times weaker than the 337 nm line of N_2, the initial populations of excited and ionized N_2 molecules are comparable after nonradiative relaxation channels are accounted for, demonstrating that nitrogen plasma is generated.

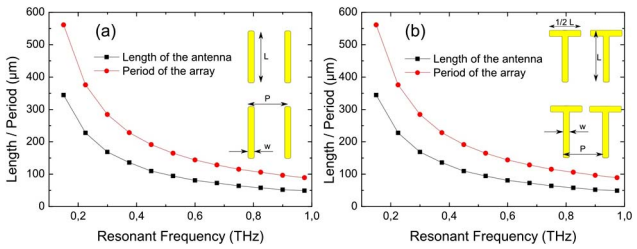

Fig. 2. Optimized design of lengths and periods of resonant dipole antennas on HR-Si for (a) I-shape and (b) T-shape structures. The width of all the antennas is kept constant at $w = 5$ μm, and the thickness of the gold layer is $d = 200$ nm.

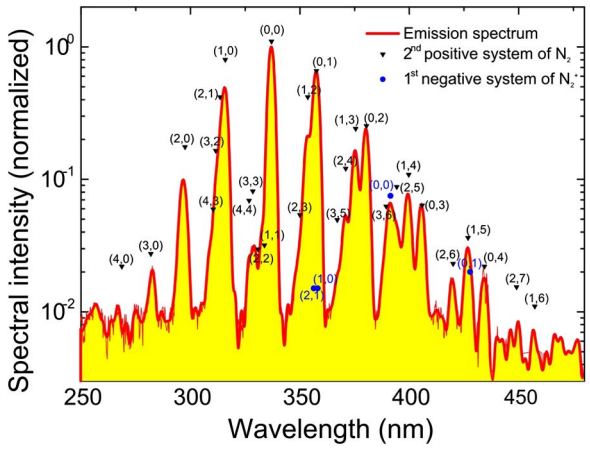

Fig. 3. Intensity spectrum of the detected UV light. Markers show positions and radiative strengths of the second positive system of excited N_2 ($C^3\Pi_u$ to $B^3\Pi_g$ transition) and the first negative system of excited N_2^+ ($B^2\Sigma_u^+$ to $X^2\Sigma_g^+$ transition) [22]. Numbers on the plot indicate initial and final vibrational states of the molecule.

UV emission from plasma has recently been observed from nanoantennas illuminated with 800 nm radiation at TW/cm^2 intensities [23]. It is believed that nanostructure-enhanced multiphoton and strong-field excitation and ionization of atomic gas is responsible for the generation of nanoplasma. In our experiment, though, free electrons are essential.

To demonstrate that it is the electrons emitted from the metal that initiate the plasma generation process and it is not a direct effect of the strong electric field on the N_2 molecule, we covered the sample with a 55-nm-thin layer of electrically insulating silicon dioxide (SiO_2) by plasma enhanced chemical vapor deposition [Fig. 4(a)]. The field enhancement for both a bare sample and one covered with SiO_2 are shown in Fig. 4(b). Even though the peak electric field outside the structure covered with SiO_2 (point B) is higher than for the bare structure (point A), no UV emission above the noise level (10^{-4} of the signal) was detected.

Additionally, if an antenna sample is placed in a vacuum, no UV emission is detected, as shown in Fig. 5(a). To exclude the influence of the substrate in the UV light generation process, we have fabricated an additional set of samples on a fused-silica substrate. These samples showed UV emission with the same properties as for those on the HR-Si substrate.

The dynamics of UV emission [Fig. 5(b)] reveal that the UV emission happens on the nanosecond time scale. For pure

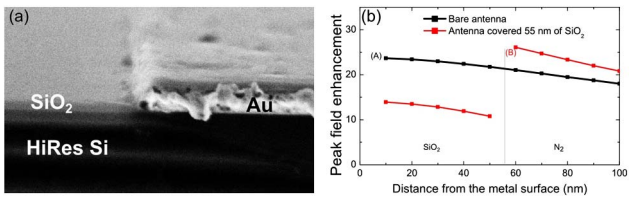

Fig. 4. (a) SEM cross-sectional image of sample covered with 55 nm thick layer of isolating SiO_2. Black/dark gray, HR-Si; bright gold/gray, SiO_2 (b) Simulation of peak time-domain field enhancement as a function of distance from the metal surface for bare sample and sample covered with 55 nm of SiO_2.

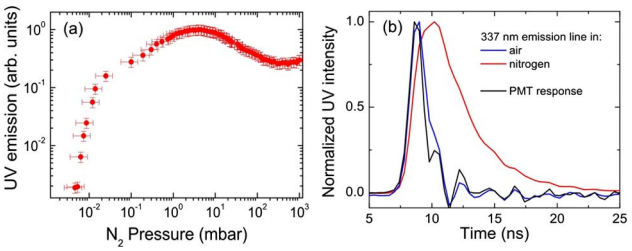

Fig. 5. (a) Intensity of UV emission at 337 nm as a function of pressure of the gas surrounding THz resonant antenna. The sample is in a vacuum chamber, which is pumped out while monitoring UV emission and gas pressure. (b) UV emission in both dry atmospheric air and pure nitrogen. The response time of the PMT used in the experiment is too slow to fully investigate the dynamics of UV emission in air, but it is fast enough to resolve it in pure nitrogen. PMT response is measured by illumination with a 400 nm 100 fs pulse.

nitrogen gas at atmospheric conditions the radiative time is 3 ns, while for atmospheric air radiative time it is only 1 ns.

UV radiation is emitted from the regions near the antenna tips as shown in Figs. 6(c) and 6(f). The individual spots have an approximately circular shape with a 10–15 μm diameter full width at half maximum (FWHM), which is slightly larger than the resolution of the imaging optics (9 μm). That indicates that the UV emission occurs in a few micrometer-large volume of space surrounding the antenna tips, although to undoubtedly verify that statement an imaging setup with better spatial resolution is necessary.

The symmetry of the system with respect to the electric field is broken by the sign of electron charge, with electron emission expected from a given point on the antenna only when the electric field is pointing towards the metal. This prediction is verified by our measurement of the emitted UV intensity as a function of the angle between the linear THz polarization and the main axis of the antenna (Fig. 7), where a 180° rotation corresponds to a sign change of the field (or phase change of the THz wave by π). As expected, the total UV emission for the I-shape antenna is symmetric with respect to the sign of the THz field. However, the UV emission for the T-shape antenna is highly asymmetric with respect to the sign of the THz field.

These results agree with the field enhancement of the antennas from computer simulation. As expected, the field enhancement at each end of the symmetric I-shape antenna is identical [Fig. 6(b)], but the asymmetric T-shape has a field enhancement at the bottom tip that is substantially higher than that of the upper tips [Fig. 6(e)], causing increased plasma formation in that region. When parallel to the electric field, 70% of the UV radiation is emitted from the bottom tip of the T. It is worth noting that this analysis is only possible due to the single-cycle nature of the THz pulse, its intrinsic CEP stability, and the sensitivity of the process to the time-domain electric field strength [Fig. 1(d)].

4. MODELING—FOUR-STEP MODEL

To explain the observed UV emission we propose a simple four-step model, shown schematically in Fig. 8. The first step is the ultrafast electron field emission from the metal, modeled

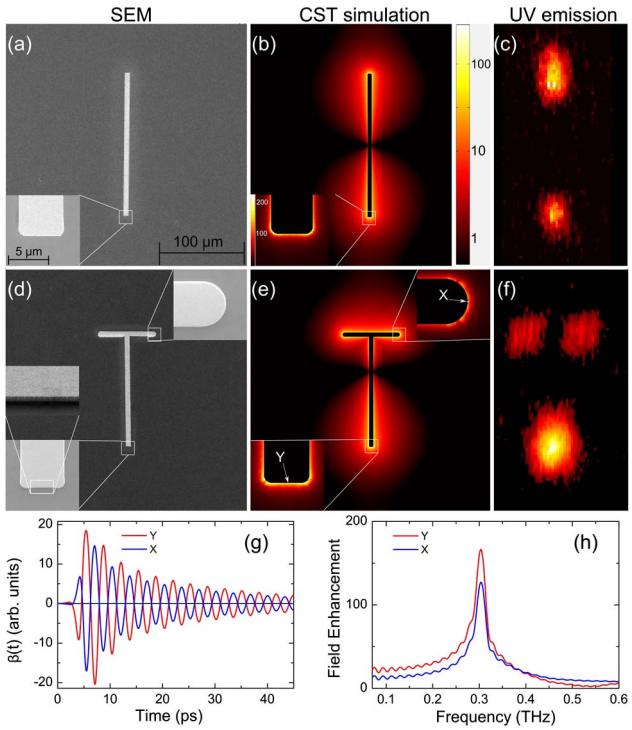

Fig. 6. I-shape and T-shape antennas for electron field emission fabricated by standard UV lithography. (a), (b) Scanning electron micrograph images of a unit cell for (a) I-shape and (d) T-shape antennas optimized for 0.3 THz on a high-resistivity silicon (HR Si) substrate. The inset shows the gold surface topology with visible irregular grains in the 20–100 nm size range. Full-wave numerical simulations of the field amplitude enhancement on a logarithmic scale at the resonant frequency for (b) I-shape and (e) T-shape antennas. The inset shows a close-up on a linear scale of the field enhancement at the tips. (c), (f) Experimentally determined UV emission patterns. The spatial scale on all the (a)–(f) plots is kept fixed; thus the position of UV emission is directly comparable to the SEM image and numerical simulation. (g) Time-domain and (h) frequency-domain β field enhancement of surface field at the X and Y points of a T-shape antenna.

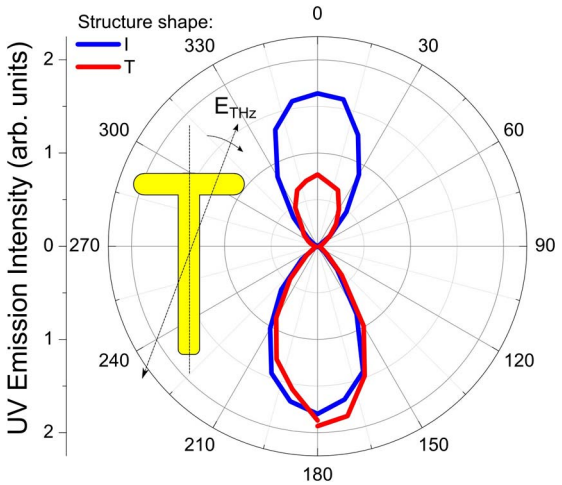

Fig. 7. UV emission intensity as a function of the polarization direction of the incident THz transient indicating symmetry breaking of the emission pattern due to the sign of the electron charge and asymmetry of the THz pulse.

by the Fowler–Nordheim (F-N) equation [24,25], which depends on the incident electric field, the time-domain surface field enhancement, and the work function of the metal Φ. The local electric field at the metal surface tilts the potential barrier and allows electrons to tunnel through it. Since the tunneling process is much faster than the oscillation of the THz field, the liberated electron is then exposed to the same external electric field that caused the tunneling and the electron is accelerated out of the high field region in the subcycle regime before the THz field changes sign. This acceleration, which can be modeled classically, imparts substantial kinetic energy to the electron, which then propagates undisturbed until it scatters on an N_2 molecule. Assuming elastic scattering at atmospheric pressure [26] this event takes place approximately 150 fs after emission and gives the electron a random propagation direction. If the electron acquired enough kinetic energy prior to collision, it can excite and/or ionize an N_2 molecule (12 and 15 eV thresholds). The radiative lifetime of the excited N_2 molecule in the $C^3\Pi_u$ state is 39 ns (60 ns for $B^2\Sigma_u^+$ state) [27]. A competing, nonradiative channel involves collisions with other nitrogen molecules and efficiently depopulates the excited state and decreases the effective radiative lifetime [28] to 3 and 0.1 ns, respectively.

Below we present more thorough description of the four-step model introduced in the paper. Steps 1 and 2 are very similar to the Simpleman model [10,29,30].

A. Step ①

The first step of our model is electron field emission [24,25,31], which expresses the electron field emission current density J in the form

$$J = \alpha_M \lambda_C a(\beta E_0)^2 \Phi^{-1} \exp\left(-\frac{v b \Phi^{\frac{3}{2}}}{\beta E_0}\right),$$

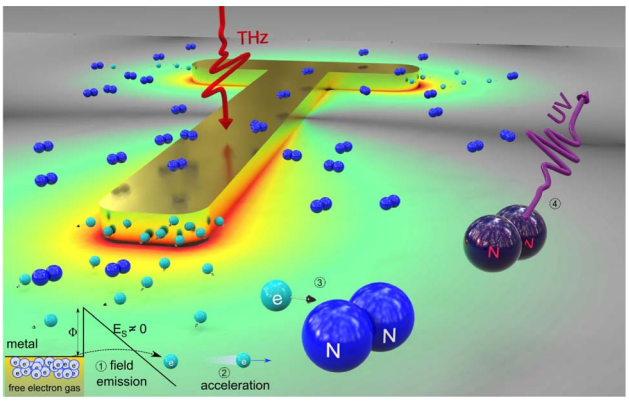

Fig. 8. Ultrafast electron field emission, generation of nitrogen plasma, and emission of UV radiation using ultrashort high-power THz transients. Step ①, field-induced electron emission. Surface electric field E_s induced by the THz wave tilts the potential outside the metal, thus allowing electrons to tunnel through the potential barrier Φ. Step ②, the external THz electric field accelerates the electrons, which acquire kinetic energy up to 100 eV. Step ③, electrons collide with molecular nitrogen and generate nitrogen plasma (mix of molecules in excited and ionized states). Step ④, nitrogen molecules emit UV radiation and relax to a lower energy state.

where $a = 1.53 \cdot 10^{-6}\,\mathrm{AeVV^{-2}}$ and $b = 6.829 \cdot 10^{9}\,\mathrm{eV^{-3/2}Vm^{-1}}$ are the first and second F-N constants, v is a correction factor associated with the barrier shape, λ_C is a characteristic supply correction factor, α_M is the area efficiency of emission, Φ is the work function of the metal, β is the local field enhancement factor, and E is the incident macroscopic electric field. We simplify the barrier shape as triangular, which yields $\alpha_M = \lambda_C = v = 1$. The total emitted charge Q can be calculated by integrating J over the antenna surface and in time. For simplicity we assume that the emission density is constant over the tip of the antenna, and we multiply the current density by the area of the antenna tip $(w \cdot d)$ to obtain the emission current. Due to the surface irregularities, the effective emission area is smaller than the macroscopic area of the device.

From the computer simulation we obtain the time-domain field enhancement $\beta(t)$ at the tip of the antenna, which, together with the peak incident THz field of $E_0 = 200$ kV/cm, allows us to calculate the emission current from each tip of the antenna. In that process we assume the value of the work function of the metal. We find that the effective work function for our system is $\Phi = 0.25 \pm 0.03$ eV. As the system is excited, electrons are emitted in short bunches. The electron emission location alternates between the top and bottom tips of the antenna depending on the direction of the surface electric field. Because the electron field emission is strongly nonlinear, only a few electron bunches are emitted even though the electric field at the antenna oscillates for many picoseconds. As shown above, covering one tip of the antenna with SiO_2 would result in emission of a single electron bunch.

The application of the F-N equation is justified due to the extremely low value of the Keldysh parameter. Values of the Keldysh parameter and other characteristic parameters are summarized in Table 1 for the antenna samples with the highest and lowest time-domain field enhancements.

B. Step ②—Electron Ballistic Acceleration

After an electron tunnels through the potential barrier it experiences the external electric field that led to the tunneling. The external electric field, which rapidly decreases in strength away from the antenna tip, accelerates the electron. This step is modeled by simple ballistic acceleration where the position, speed, kinetic energy, and acceleration of electrons emitted from the antenna tip are calculated as a function of time after tunneling and the local value of the electric field. For simplicity we assume that acceleration stops when the electron scatters on a N_2 molecule. During the ballistic acceleration, electrons can gain up to 100 eV of kinetic energy [Fig. 10(b)]. As a point of reference, we have also calculated the ponderomotive energy the electrons would obtain if they were continually exposed to the peak electric field, as opposed to being accelerated into a lower field region. These values are presented in Table 1 as "peak ponderomotive energy" along with the quiver amplitude and δ parameter [10] for these peak energy values. Again, these peak values are not achieved due to quenching by the strong spatial gradient of the enhanced electric field.

Table 1. Summary of Several Characteristic Parameters for the Samples with Highest and Lowest Time-Domain Field Enhancements

Parameter	0.6 THz I-Shape Antenna	0.15 THz I-Shape Antenna
Max field enhancement β_{max}	32	14
Max surface electric field ($\beta_{max}E_0$)	$32 \cdot 200$ kV/cm $= 6.4$ MV/cm	$14 \cdot 200$ kV/cm $= 2.8$ MV/cm
Local peak field intensity	100 GW/cm^2	19 GW/cm^2
Tunneling frequency (assuming $\Phi = 0.25$ eV)	49 THz	21.6 THz
Keldysh parameter for tunneling electron	0.012	0.007
Peak ponderomotive energy	1.3 keV	3.9 keV
Quiver amplitude	7.9 μm	55 μm
δ parameter (field decay length/Quiver amplitude)	0.025	0.0036

C. Step ③—Excitation and Ionization of N_2 Molecule

Figure 9(a) shows the scattering cross sections for electrons and N_2 molecules for three different processes: elastic scattering, excitation of the $C^3\Pi_u$ state, and ionization of N_2 to the $B^2\Sigma_u^+$ state [26]. The electron kinetic energy threshold for excitation of N_2 to the $C^3\Pi_u$ state is 12 eV, and 15.6 eV for ionization of N_2 to $B^2\Sigma_u^+$. Figure 9(b) shows the scattering time of those three processes for nitrogen gas at atmospheric pressure. The elastic scattering time constant is 150 fs for electrons with energy above 12 eV so that, statistically, the electron will scatter elastically 150 fs after field emission and then randomly change propagation direction. Due to the high ratio between the mass of an electron and an N_2 molecule, elastic scattering does not significantly change the energy of the electron. On the other hand, inelastic scattering, which leads to excitation of the $C^3\Pi_u$ state, happens approximately 3 ps after field emission. In this time, electrons are elastically scattered many times and have traveled several micrometers away from the emission area. The FWHM of diffusion of electrons is estimated to be 17 μm based on the random walk equation and could contribute to the size of UV emission centers in Figs. 6(c) and 6(f).

D. Step ④—UV Emission

When N_2 is excited to the $C^3\Pi_u$ state, it has a lifetime of 39 ns before emitting a UV photon unless deexcited through another process [27,28], the most likely of which is a collision with another molecule. For pure nitrogen gas at atmospheric conditions, collisions with other N_2 molecules decrease the effective radiative time to 3 ns. For atmospheric air with 20.8% O_2, like that in the experimental conditions, this process is even more efficient and the effective radiative time is reduced to only 1 ns [Fig. 5(b)]. As a result, the number of measured UV photons corresponds to only a fraction of the excited N_2 molecules. The diffusion of excited nitrogen molecules away from the antenna tip is estimated on the order of 1.5 μm.

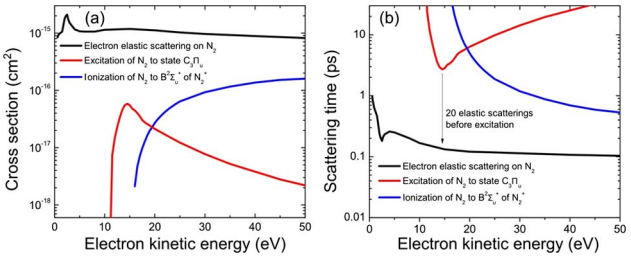

Fig. 9. (a) Cross section for electron collisions with nitrogen molecules for various processes. Adapted from [26]. (b) Calculated time between scatterings of electrons with nitrogen molecules at atmospheric pressure for various processes.

5. DISCUSSION

To verify the proposed four-step model we present the detected UV intensity as a function of the incident THz field strength [Fig 10(a)]. The calibrated THz → UV energy conversion efficiency reaches 10^{-5}, which is relatively high considering that the THz-induced UV generation would be a 1000-photon process in the multiphoton picture. The inset of Fig. 10(a) shows plots of $\ln(I/E_{av}^2)$ versus $1/E_{av}$, where E_{av} is the photon-averaged incident electric field. The time-domain field enhancement factor β can be calculated from the slopes of those plots [32,33]. The field enhancement factor in that calculation depends on the assumed height of the tunneling barrier Φ, and convincing agreement between experiment and numerical simulations is obtained for $\Phi = 0.25 \pm 0.03$ eV [Fig. 10(c)].

One of the controversial issues is the value and meaning of the potential tunneling barrier Φ in the THz regime. Cocker *et al.* [9] show in their recent THz-STM experiment that this value for gold in air is 0.2 eV, which is significantly lower than the work function for gold (5.0 eV). Our value (0.25 ± 0.03 eV) is in agreement with these THz-STM measurements, although the mechanism may be different. In the case of THz-STM measurements in air, adsorbates can open up channels across the gap at energies much lower than the vacuum level [34]. This can lead to the unusually low work functions.

We suspect that a combination of two effects is responsible for the extraordinarily low value of the potential barrier in our case. The first is the previously mentioned contribution from adsorbates and other impurities from air on the gold surface. It is well known that surface adsorbates can significantly lower the work function of a metal for electron field emission [35], though it is rather unlikely that this effect alone can reduce the work function to the sub-eV level.

The second effect is the local field enhancement due to the surface topology of the gold. From analyzing SEM images of our samples it is clear that the vertical surfaces of our antennas are highly irregular on the submicrometer scale [Fig. 6(d)]. Small dents, nanoislands, and other surface irregularities can provide significant local field enhancements on the few-nanometer length scale. Recall that the β factor in the F-N equation is the total field enhancement, which has two contributions. One contribution is the macroscopic field enhancement from the antenna itself, and there is a second contribution from the local surface topology. Since the shape of the F-N plot [inset to Fig. 10(a)] is invariant with the $\Phi^{3/2}/\beta$ factor, any underestimation of β will manifest itself as a decrease of the potential

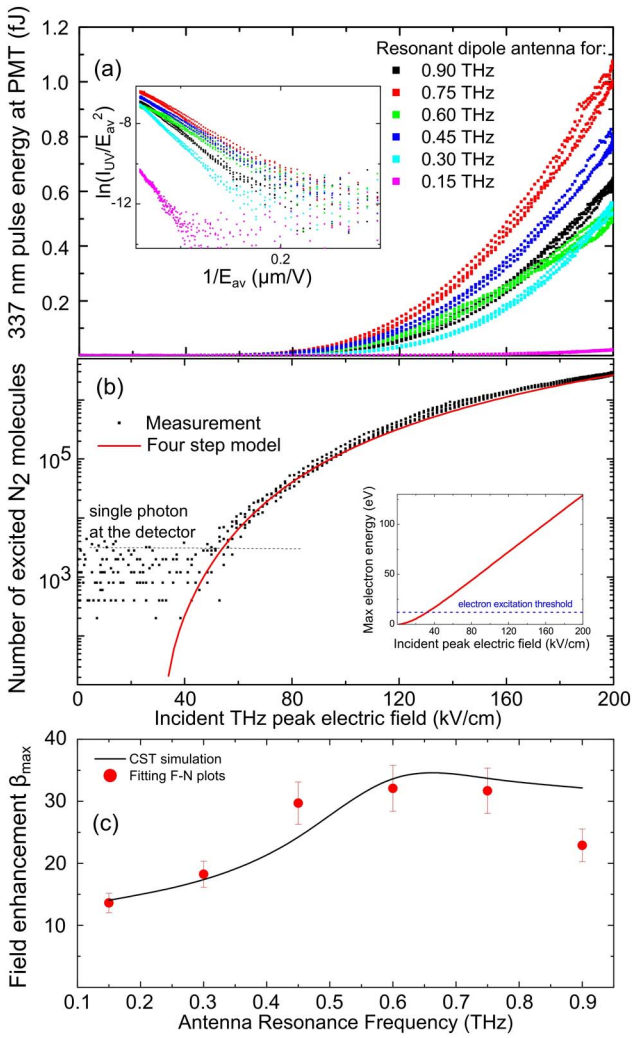

Fig. 10. UV emission from various length antenna structures illuminated with THz radiation. (a) 337 nm pulse energy detected by a PMT at the position of 60 mm away from the sample as a function of the incident peak THz field for I-shape antennas with various resonant frequencies. The inset shows the corresponding F-N plots displayed as $\ln(I_{UV}/E_{av}^2)$ versus $1/E_{av}$. (b) Measurement and four-step model simulation of the number of the excited N_2 molecules as a function of the incident peak electric field. The inset shows simulation of the maximum electron kinetic energy before it elastically scatters off an N_2 molecule. (c) CST time-domain simulation of the field enhancement at the surface of the tip of the antenna and estimation of the field enhancement based on the F-N plot for various I-shape antennas.

barrier Φ [32]. Our experiment cannot resolve these local field enhancement factors, and we instead use the value obtained directly from simulation for perfectly smooth surfaces. As a result, the tunneling barrier we determine is an effective work function for a given surface topology seen from a macroscopic perspective.

This unusually low potential barrier is beneficial for field emission and allows up to 10^6–10^7 emitted electrons per pulse. Based on the number of detected UV photons and the radiative and nonradiative depopulation of the $C^3\Pi_u$ state, the total number of excited N_2 molecules can be determined [Fig. 10(b)]. The same graph summarizes the results of the four-step model simulation, which is in close quantitative agreement with the experimental data. Our numerical simulations show that the maximum achievable electron energy is on the order of 100 eV for the highest THz electric field strengths used.

6. CONCLUSIONS

In conclusion we have demonstrated that a strong THz pulse can generate ultrafast field emission of electrons from a metal surface via nonperturbative nonlinear interactions. The electrons are accelerated to multi-10-eV kinetic energies by the same enhanced THz field near the metal. Our results pave the road towards novel low-energy electron sources that are ideally suited for surface-near electron loss and electron diffraction time-resolved studies in physics, chemistry, and biology. We showed that the emitted electrons can initiate collision-induced physical processes on an ultrafast time scale, here illustrated by formation of a nitrogen plasma. This mechanism forms the basis for compact THz detectors that measure the intensity of THz-induced UV emission. Such a detector, unlike those currently available, is sensitive to the peak THz field in an ungated manner and thus offers new detection capabilities akin to nonlinear optical detectors in the visible and near-infrared.

REFERENCES

1. J. Kupersztych, P. Monchicourt, and M. Raynaud, "Ponderomotive acceleration of photoelectrons in surface-plasmon-assisted multiphoton photoelectric emission," Phys. Rev. Lett. **86**, 5180–5183 (2001).
2. R. J. D. Miller, R. Ernstorfer, M. Harb, M. Gao, C. T. Hebeisen, H. Jean-Ruel, C. Lu, G. Moriena, and G. Sciaini, "'Making the molecular movie': first frames," Acta Crystallogr. Sect. A **66**, 137–156 (2010).
3. D. J. Flannigan and A. H. Zewail, "4D electron microscopy: principles and applications," Acc. Chem. Res. **45**, 1828–1839 (2012).
4. C. Ropers, D. R. Solli, C. P. Schulz, C. Lienau, and T. Elsaesser, "Localized multiphoton emission of femtosecond electron pulses from metal nanotips," Phys. Rev. Lett. **98**, 043907 (2007).
5. M. Schenk, M. Krüger, and P. Hommelhoff, "Strong-field above-threshold photoemission from sharp metal tips," Phys. Rev. Lett. **105**, 257601 (2010).
6. G. Wachter, C. Lemell, J. Burgdörfer, M. Schenk, M. Krüger, and P. Hommelhoff, "Electron rescattering at metal nanotips induced by ultrashort laser pulses," Phys. Rev. B **86**, 035402 (2012).
7. M. Krüger, M. Schenk, and P. Hommelhoff, "Attosecond control of electrons emitted from a nanoscale metal tip," Nature **475**, 78–81 (2011).
8. L. Wimmer, G. Herink, D. R. Solli, S. V. Yalunin, K. E. Echternkamp, and C. Ropers, "Terahertz control of nanotip photoemission," Nat. Phys. **10**, 432–436 (2014).
9. T. L. Cocker, V. Jelic, M. Gupta, S. J. Molesky, J. A. J. Burgess, G. D. L. Reyes, L. V. Titova, Y. Y. Tsui, M. R. Freeman, and F. A. Hegmann, "An ultrafast terahertz scanning tunnelling microscope," Nat. Photonics **7**, 620–625 (2013).
10. G. Herink, D. R. Solli, M. Gulde, and C. Ropers, "Field-driven photoemission from nanostructures quenches the quiver motion," Nature **483**, 190–193 (2012).
11. R. Bormann, M. Gulde, A. Weismann, S. V. Yalunin, and C. Ropers, "Tip-enhanced strong-field photoemission," Phys. Rev. Lett. **105**, 147601 (2010).

12. P. Hommelhoff, Y. Sortais, A. Aghajani-Talesh, and M. A. Kasevich, "Field emission tip as a nanometer source of free electron femtosecond pulses," Phys. Rev. Lett. **96**, 077401 (2006).
13. K.-L. Yeh, M. C. Hoffmann, J. Hebling, and K. A. Nelson, "Generation of 10 μJ ultrashort terahertz pulses by optical rectification," Appl. Phys. Lett. **90**, 171121 (2007).
14. M. C. Hoffmann and J. A. Fülöp, "Intense ultrashort terahertz pulses: generation and applications," J. Phys. D **44**, 083001 (2011).
15. H. Hirori, A. Doi, F. Blanchard, and K. Tanaka, "Single-cycle terahertz pulses with amplitudes exceeding 1 MV/cm generated by optical rectification in $LiNbO_3$," Appl. Phys. Lett. **98**, 091106 (2011).
16. K. Iwaszczuk, A. Andryieuski, A. Lavrinenko, X.-C. Zhang, and P. U. Jepsen, "Terahertz field enhancement to the MV/cm regime in a tapered parallel plate waveguide," Opt. Express **25441**, 25441–25448 (2011).
17. C. Winnewisser, P. U. Jepsen, M. Schall, V. Schyja, and H. Helm, "Electro-optic detection of THz radiation in $LiTaO_3$, $LiNbO_3$ and ZnTe," Appl. Phys. Lett. **70**, 3069–3071 (1997).
18. Q. Wu, M. Litz, and X.-C. Zhang, "Broadband detection capability of ZnTe electro-optic field detectors," Appl. Phys. Lett. **68**, 2924–2926 (1996).
19. A. Nahata, D. H. Auston, T. F. Heinz, and C. Wu, "Coherent detection of freely propagating terahertz radiation by electro-optic sampling," Appl. Phys. Lett. **68**, 150–152 (1996).
20. P. Klarskov, A. C. Strikwerda, K. Iwaszczuk, and P. U. Jepsen, "Experimental three-dimensional beam profiling and modeling of a terahertz beam generated from a two-color air plasma," New J. Phys. **15**, 075012 (2013).
21. J. Dai, J. Zhang, W. Zhang, and D. Grischkowsky, "Terahertz time-domain spectroscopy characterization of the far-infrared absorption and index of refraction of high-resistivity, float-zone silicon," J. Opt. Soc. Am. B **21**, 1379–1386 (2004).
22. A. Lofthus and P. H. Krupenie, "The spectrum of molecular nitrogen," J. Phys. Chem. Ref. Data **6**, 113–307 (1977).
23. M. Sivis, M. Duwe, B. Abel, and C. Ropers, "Extreme-ultraviolet light generation in plasmonic nanostructures," Nat. Phys. **9**, 304–309 (2013).
24. R. H. Fowler and L. Nordheim, "Electron emission in intense electric fields," Proc. R. Soc. A **119**, 173–181 (1928).
25. R. G. Forbes, "Physics of generalized Fowler-Nordheim-type equations," J. Vac. Sci. Technol. B **26**, 788–793 (2008).
26. Y. Itikawa, "Cross sections for electron collisions with nitrogen molecules," J. Phys. Chem. Ref. Data **35**, 31–53 (2006).
27. F. Valk, M. Aints, P. Paris, T. Plank, J. Maksimov, and A. Tamm, "Measurement of collisional quenching rate of nitrogen states N_2 ($C^3\Pi_u$, v = 0) and N_2^+ ($B^2\Sigma_u^+$, v=0)," J. Phys. D **43**, 385202 (2010).
28. K. V. Kozlov, R. Brandenburg, H.-E. E. Wagner, A. M. Morozov, and P. Michel, "Investigation of the filamentary and diffuse mode of barrier discharges in N_2/O_2 mixtures at atmospheric pressure by cross-correlation spectroscopy," J. Phys. D **38**, 518–529 (2005).
29. P. Corkum, "Plasma perspective on strong field multiphoton ionization," Phys. Rev. Lett. **71**, 1994–1997 (1993).
30. G. Paulus, W. Becker, and H. Walther, "Classical rescattering effects in two-color above-threshold ionization," Phys. Rev. A **52**, 4043–4053 (1995).
31. R. G. Forbes, "On the need for a tunneling pre-factor in Fowler–Nordheim tunneling theory," J. Appl. Phys. **103**, 114911 (2008).
32. R. Gomer, "Field emission, field ionization, and field desorption," Surf. Sci. **299**, 129–152 (1994).
33. Z. Zhang, G. Meng, Q. Wu, Z. Hu, J. Chen, Q. Xu, and F. Zhou, "Enhanced cold field emission of large-area arrays of vertically aligned ZnO-nanotapers via sharpening: experiment and theory," Sci. Rep. **4**, 4676 (2014).
34. C. J. Chen, *Introduction to Scanning Tunneling Microscopy* (Oxford University, 1993).
35. C. B. Duke, "Field emission through atoms adsorbed on a metal surface," J. Chem. Phys. **46**, 923–937 (1967).